Anhydrous Calcium Oxalate Polymorphism: a combined computational and synchrotron X-ray diffraction study.

Wen Zhao[1], Neeraj Sharma[2], Franca Jones[3], Paolo Raiteri[1], Julian D. Gale[1], Raffaella Demichelis[1,]*

[1]Curtin Institute for Computation, The Institute for Geoscience Research, and Department of Chemistry, Curtin University, GPO Box U1987, Perth, Western Australia 6845, Australia

[2]School of Chemistry, University of New South Wales, Sydney, New South Wales, Australia.

[3]Nanochemistry Research Institute and Department of Chemistry, Curtin University, GPO Box U1987, Perth, Western Australia 6845, Australia.

KEYWORDS: Anhydrous Calcium Oxalate (COA), IR spectrum, DFT, polymorphism, variable temperature X-ray diffraction

ABSTRACT

Four possible models for anhydrous calcium oxalate (COA) polymorphs have been investigated through *ab initio* quantum mechanical methods. Their structural properties, IR and Raman spectra, and thermodynamic stability in the range of 0-800 K have been analyzed and compared. Along with the known β-COA structures, two models turn out to be possible candidates for the α- and γ- polymorphs that

were observed during dehydration of weddellite (calcium oxalate dihydrate, COD) by Walter-Lévy and Laniepce (C. R. Acad. Sc. Paris, 259, 4685, 1964). While the calculated vibrational frequencies show that the four COA models correspond to minimum energy structures, β-COA is the thermodynamically favored phase over the range of temperatures examined in the present study. Despite the fact that computed vibrational spectra and XRD patterns of these polymorphs exhibit some different features, a definitive assignment of the structures based on computational results is not possible due to the lack of accurate experimental data. In an effort to improve comparative experimental data, the structural evolution of whewellite (calcium oxalate monohydrate, COM) has been probed using time-resolved synchrotron X-ray diffraction, in order to correlate the calculated structures to the observed structures. The evolution has been shown to go through at least 4 phases identified as COM, α-COA (corresponding to one of the models proposed by computation), β-COA, and $CaCO_3$. The reactions are predominantly two-phase reactions and at 140 °C evidence of three-phase co-existence has been noted between COM, α-COA, and β-COA. The time-resolved XRD data allow estimation of the kinetics of the reactions; these indicate second order reactions between COM and α-COA and zeroth order reactions between α-COA and β-COA.

Introduction

Biomineralization is the process by which living organisms produce minerals, and it is an extremely widespread phenomenon in nature.[1-3] In recent years, research in this field has seen an increased focus on aspects related to human health. Specifically, an imbalance in the mineralization/demineralization equilibria, the basis of the formation and maintenance of human hard tissues, can result in health problems, as well as in the formation of some undesired minerals in the body. One such example is the formation of kidney stones, which are commonly composed of calcium oxalate. Because of this, and together with the fact that calcium oxalate is frequently found as a biomineral in plants, research into the phases of calcium oxalate, including its hydrates, is attracting significant attention.[4-14] Various forms of hydrated calcium oxalate have been identified by experimental techniques, namely calcium oxalate monohydrate (whewellite, $CaC_2O_4 \cdot H_2O$, COM), calcium oxalate dihydrate (weddellite, $CaC_2O_4 \cdot (2+x)H_2O$, $x \leq 0.5$, COD) and calcium oxalate trihydrate (caoxite, rarely observed, $CaC_2O_4 \cdot 3H_2O$, COT).[4,6,15-20] As in the case of calcium carbonate, an amorphous phase has also been detected for calcium oxalate, with a degree of hydration close to 1 molecule of water per formula unit.[21,22] On the other hand, understanding the structure and polymorphism of anhydrous calcium oxalate (COA) directly from experiment is a challenge due to the fact that it is highly hygroscopic and therefore little work has been done so far on these phases.

According to previous studies, three forms of COA have been identified by experimental techniques, such as thermogravimetric analysis (TGA) and X-ray diffraction (XRD). These three temperature-dependent polymorphs are known as α-, β-, and γ-COA, and were originally obtained through dehydration of COD and labeled by Walter-Lévy and Laniepce in 1964.[23]

Notably, the γ-phase was detected only when starting from COD samples ground into fine grains. Though unable to fully determine the structures, Hocart *et al*.[24] observed that while the *c* and *β* lattice parameters may change between the α- and the β-phase, the dehydration of COM is essentially topotactic, since no significant structural rearrangement was detected. However, the definition of these COA polymorphs is still controversial because of a lack of conclusive evidence. The crystal structures of α- and γ-COA are still unknown, while that of β-COA has only been reported recently through a combination of computer simulation[25], based on density functional theory (DFT) within the generalized gradient approximation (GGA) using the PBE functional, Rietveld refinement of a structural model with XRD data, and comparison with the XRD patterns recorded in Walter-Lévy and Laniepce's study.[23] Here, β-COA, was found to belong to the monoclinic space group P2/*m*, with similar *a, c*, α, γ lattice parameters as COM, while β~90º and *b* is approximately half of that for COM.

In this work we aim to investigate the structural properties of COA using *ab initio* quantum mechanical methods to examine possible candidate atomic configurations and then to correlate the determined structures to experimental observations. The key differentiator in this experimental study is the use of *in situ* variable temperature XRD. Effectively COM has been heated while XRD data have been continuously collected and then analyzed using a Rietveld approach based on the previously derived theoretical models.

Computational Methods

All calculations have been carried out with the CRYSTAL14 program.[26] Two different Gaussian-type basis sets are used; one originally optimized by Valenzano *et al*.[27] for calcite, and then successfully applied in investigating the other calcium carbonate crystalline phases (referred to

hereafter as V-BS);[28-30] the other basis set was systematically derived for the solid state by Peintinger *et al*.[31] starting from Weigend *et al*'s basis set for molecules[32,33] (subsequently referred to as pob-TZVP).

Calculations have been performed in the framework of Kohn-Sham Density Functional Theory (DFT). Various exchange-correlation functionals have been used, including the GGA functionals PBE[34] and PBEsol[35], as well as the corresponding global hybrid functionals, PBE0[36] and PBEsol0. In addition, a semiempirical GGA-type functional, PBE-D, has been applied in order to account for the long-range dispersion contribution[37]. The DFT exchange-correlation term is evaluated through numerical integration over the unit cell volume, using a pruned grid with 75 radial points and 434 angular points.

The parameters for the approximation of bielectronic integrals have been modified in order to achieve improved numerical convergence relative to the default parameters. The five parameters[38] that control the accuracy of the bielectronic Coulomb and Hartree-Fock exchange series sums have been set to 10^{-8}, 10^{-8}, 10^{-8}, 10^{-8} and 10^{-18}. Both thresholds that control the bipolar approximation of bielectronic integrals have been chosen as 10^{-18}. Reciprocal space has been sampled with a shrinking factor of 8 in all directions according to the Pack-Monkhorst[39] method. For the structures with space groups P1, P2/*m*, C2/*m* and $P2_1/c$ considered in this work, the number of points in the irreducible Brillouin zone are 260, 170, 150 and 170, respectively.

Geometry optimizations have been performed using analytical gradients with respect to both atomic coordinates and lattice parameters. A quasi-Newton optimization scheme has been adopted, combined with Broyden-Fletcher-Goldfarb-Shanno Hessian updating. The default

convergence parameters for geometry optimization have been used, with the Self Consistent Field (SCF) convergence threshold set to 10^{-8} a.u.

Harmonic vibrational frequencies at the Γ point have been calculated by diagonalizing the dynamical matrix obtained through central finite differencing of the analytical energy gradient with respect to atomic coordinates, using a displacement step of 0.003 Å. Infrared and Raman powder intensities have been calculated by a Coupled-Perturbed Hartree-Fock/Kohn-Sham (CPHF/CPKS) approach.[40-43] All Raman intensity values are normalized to the most intense peak, which is assigned a value of 1000 arbitrary units. An incoming laser wavelength of 514.5 nm[44] and a temperature of 300 K have been used for producing the Raman spectra. Constant volume heat capacity and vibrational entropy have been computed up to 800 K in order to investigate the thermodynamic stability of the four different phases. Here all terms are evaluated at the 0 K structure, without considering the contribution due to thermal expansion. Given the similarity of the unit cells, only frequencies at the Γ point have been considered. The SCF convergence threshold during frequency calculations has been set to 10^{-10} a.u.

The simulated XRD patterns have been produced with the Mercury program[45] in the range of $0 \leq 2\theta \leq 50^{\circ}$, using the equilibrium geometry optimized with V-BS and PBE0. The wavelength has been set at the experimental value of 0.99996 Å, with a step of 0.02 degree and a full width at half maximum of the Gaussian functions (FWHM) of 0.1 degree.

Experimental Methods

COM has been obtained from Alfa Aesar and was nominally 99% pure and used as received. Characterization has been performed by TGA, FTIR and XRD analysis thereby confirming the composition. Synchrotron XRD data have been collected on the Powder Diffraction beamline[46] at

the Australian Synchrotron with a wavelength (λ) of 0.99996 Å determined using the NIST 660a LaB_6 standard reference material. Data have been collected continuously in 2.4 min acquisitions in transmission geometry throughout the heating cycles and Rietveld refinements have been carried out using the GSAS[47] software suite with the EXPGUI[48] software interface.

The sample has been placed inside a 0.3 mm inner diameter quartz capillary and an FMB-Oxford (Cyberstar) hot-air blower has been used for heating. Two runs have been performed. In the first the sample has been heated to 210 °C at 2 °C/min, held at 210 °C for 20 min, heated to 360 °C at 1 °C/min, held at 360 °C for 60 min and heated to 410 °C at 1 °C/min. The second run has been undertaken with significantly longer hold times at the lower temperatures, with hold steps at 120, 130, 140, 145 and 150 °C and ramps steps of 1.5 °C/min. The longest hold has been at 140 °C for 140 min. The final heating ramp from 150 °C to 370 °C has been undertaken at 5 °C/min and the sample held at 370 °C for 140 min.

Results and discussion

Structures of COA polymorphs

The structure of β-COA as reported by Hochrein *et al*.[25] has been selected as an initial model. **Table 1** shows the final optimized lattice parameters when applying five different exchange-correction functionals and the two selected basis sets, together with a comparison with the published cell parameters of β-COA.[25] The list of functionals adopted here also includes PBE, which is the one originally used by Hochrein *et al*. As expected on the basis of previous studies,[49,50] PBE tends to overestimate the unit cell volume, whereas the other functionals provide denser structures. Overall, all functionals provide a reasonable description of the lattice

parameters and bond distances (the latter are not reported in **Table 1**). A similar comment holds when comparing the performance of the two basis sets considered here. Despite pob-TZVP being a richer, variationally superior, and systematically derived basis set, no significant difference is observed regarding its performance in describing the structural features of β-COA with respect to V-BS[27], except for pob-TZVP providing slightly denser structures. As a consequence of this initial benchmark, we decided to perform the structural analysis of the remaining phases using V-BS and the hybrid PBE0 functional.

Three structures other than β-COA (**Figure 1**) have been considered in the present study. Two, namely COA-II and COA-III, have been obtained as a result of force field calculations performed on β-COA and β-COA/water systems. The description of these calculations is outside the scope of this paper, and will be presented elsewhere; here we just focus on the resulting alternative structural models. COA-IV has been obtained by deleting the water molecules from COM[20] and re-optimizing the structure. Vibrational frequency calculations show that all these phases are minimum energy structures.

The optimized lattice parameters of the four COA structures are reported in **Table 2** and the full results from vibrational frequency calculations will be discussed in a later section. The optimized lattice parameters of COM are reported for structural comparison as well. This table shows that COA-III is the least dense phase, though the value for its density is only 2.5-3% from those of β-COA and COA-IV. COA-II is ~0.4 g/cm^3 denser (>20%) than all the other phases. In terms of structural arrangements, all structures apart from COA-II belong to a monoclinic space group (P2/*m* for β-COA and COA-III; C2/*m* for COA-IV) and have very similar lattice parameters, while COA-II has triclinic P1 symmetry.

When visualizing the structures along the crystallographic *b*-axis, as shown in **Figure 1**, two types of oxalate groups can be observed; one whose molecular plane lies in the *xz* plane (we assume that *b* is oriented along the *y*-axis), and the other whose molecular plane is perpendicular to the *xz* plane (this feature is less intuitive to visualize in **Figure 1** for COA-II, as α and $\gamma \neq 90^{o}$). Clearly the orientation of the oxalate is different in the four structures. The high density of COA-II is the result of a deformation of the α and γ lattice parameters and a consequent rearrangement of the oxalate and calcium ions into a more compact framework that is quite different from those observed for the other phases. As expected, the atomic structure of COA-IV is closely related to that of COM[20] (**Figure 1**). A comparison of the calculated X-ray diffraction patterns (XRD) of the four COA structures is also shown in the same figure.

From an experimental point of view, there are two methods to determine the behavior of COA: (a) synthesize COA and, within a selected temperature range, observe the structural evolution using XRD data, and (b) heat COM and observe the structural evolution using XRD data. Here, the latter details information about the formation of COA, while the former details its temperature dependent phase transitions. Furthermore, if an *in situ* XRD experiment is undertaken, then kinetic information about the transitions can be determined; in this case the time resolution and angular resolution (i.e. how fast and the quality of the data) has to be balanced. The focus here is on the formation of COA, in order to determine the phases that appear when dehydrating COM into COA and then into its degradation product $CaCO_3$.

The first experimental *in situ* XRD data began with a gradual ramp between 1-2° C/min to 410 °C with hold steps at 210 and 360 °C. The corresponding stacked plots of selected 2θ regions are shown in **Figure 2**a-c. Initial identification of the phases in the sample is based on the available

literature,[23,25] with selected COM reflections indexed in **Figure 2**a. The phase evolution described in the literature indicates an α-phase (α-COA) up to 250 °C, followed by β-COA to 410 °C and then a transition to a γ-phase (γ-COA), the latter observed only if the dehydration is performed starting from finely ground COD samples. If this assignment is applied, the designations appear as shown in **Figure 2**a-c.

Interestingly, the transitions are fast and there is no dwell time required at these temperatures. α-COA appears at 132 °C and persists to 185 °C and if one considers the arguments above this phase may intuitively represent the first stage of COM losing H_2O, or the COA-IV structure. Both transitions to α- and β-COA are first order phase transitions (two-phase reaction). However, as shown in the color plots (**Figure 2**a-c), there is clearly a two-phase or three-phase co-existence with α-COA, as it appears with either COM, or β-COA, or both phases.

β-COA appears at 155 °C and there seems to be a subtle transition to the γ-phase. This is evidenced in **Figure 2**c, where a reflection increases in 2θ value with increased temperature (contraction of the cell) while another reflection essentially maintains its 2θ value. This evidence in favor of the existence of γ-COA may indeed be a result of anisotropic thermal evolution of β-COA rather than the transition into another phase. **Figure 2**a also shows the non-uniform changes in 2θ values of β-COA with temperature. On the other hand, the structural similarities found through computer modeling indicate that the phases might be very similar and differentiation with powder XRD data alone might be difficult. **Figure 2**b shows the final stage at higher temperatures, when COA decomposes to $CaCO_3$.

In order to isolate the α-phase and to determine its relationship to the calculated structures, a significantly slower second experiment has been undertaken (**Figure 2**d-e) and hold steps have been applied at critical temperatures below 150 °C. Reflections of β-COA appear at lower temperatures in this case (e.g. at the beginning of the 140 °C step, after 15 min at 120 °C, and 20 min at 130 °C), and the COM phase persisted to near the end of the 140 °C step. This suggests that α-COA cannot be isolated as it begins to transform into β-COA as soon as it forms.

Evidence for γ-COA is essentially non-existent in this run and the evolution to the $CaCO_3$ begins at about half way through the 370 °C step. Therefore, based on these data, we cannot conclusively indicate that a γ-phase actually exists.

To illustrate the evolution of the three phases (COM, α- and β-COA) during the 140 °C step, selected XRD patterns at the beginning, end and during are shown in **Figure 2**d-e, and Figure S1 of the Supplementary Information shows a Rietveld refined fit to COM at room temperature. The COM phase shows predominantly a decrease in reflection intensity with minor changes in the 2θ position during the course of the 140 °C step whereas both α- and β-COA show increases in the reflection intensity and shifts in 2θ position. The latter is unusual as during an isothermal step the phases appear to go through both a two-phase reaction in addition to a solid solution reaction (at least for some reflections). The combination of runs and the evolution of the α-phase suggest it is a kinetically stabilized phase. In any case, the presence of 3 phases co-existing in such a manner makes structural refinements difficult and thus calculations are required. It also raises the question of phase distribution in the sample; is it one particle with three components, a core and two shells, or is the phase distribution across particles?

A comparison of the models derived from the calculations with the reflections observed experimentally in the three phase co-existence region indicates that the α-phase is most closely related to COA-III and the β-phase is the one determined by Hochrein *et al*.[25] The optimized structures of β-COA and of COA-III as shown in **Table 2** have been used as initial models for the refinements. It should be noted that lattice parameters and some atomic coordinates have been refined to fit the XRD data. Unfortunately, full Rietveld analysis has not been possible due to the multiple phases present in the XRD data and their very similar structures (as demonstrated by the calculations). Regions with two-phases have also been considered, but they have proved to be too complex for a full refinement (i.e. with atomic parameters being refined). The Rietveld-refined fit is shown in **Figure 3**a with the inset showing a characteristic region. The lattice parameters at 100 minutes into the data collection, at about 40 minutes into the 140 °C step when all three phases co-exist (β-COA appears) are COM a = 6.29903(9), b = 14.63324(13), c = 10.10739(25) Å and β = 109.0186(18)° in monoclinic $P2_1/c$, COA-III ("α") a = 6.19853(29), b = 7.3875(5), c = 9.6193(11) Å and β = 83.914(14)° in monoclinic $P2/m$ and β-COA (refined and then fixed in this dataset) is a = 6.107, b = 7.382, c = 9.62 Å and β = 83.59° in monoclinic $P2/m$.

Figure 3b-c show the phase evolution during heating. For COM the a, c, and β lattice parameters contract while the b lattice parameter expands. Similar anisotropic lattice evolution with temperature is noted for the β-COA, with b and c increasing while a and the β angle decreases. Most of the lattice parameters stabilize at the 370 °C step with the exception of a, which continues to decrease. In terms of phase fraction, COM disappears and α-COA shows the largest

increase at 140 °C and a small proportion of β-COA is formed. The latter becomes larger in phase fraction than α-COA during the ramp to 370 °C.

The shaded regions in **Figure 3**a are where the phase fractions or quantity of the COM and β phases were relatively low such that the determination of the lattice parameters showed some variation. At the point "A" the phase fraction of α-COA is reduced to 0 then the darker blue symbols represent the phase fraction of β-COA while the lighter blue symbols are with α-COA still in the refinements but with fixed lattice parameters in this region. In both methods of fitting (with α- and β-COA or with β-COA only) after point "A" the lattice parameters of the β-COA phase are stable and the only difference appears to be in the slight decrease in β-COA phase fraction, which is related to the formation of the $CaCO_3$ phase. It should also be noted that this transformation appears to be close to a first order phase transition. The question of whether β-COA transforms to the "γ" phase still remains unanswered.

Time-resolved XRD data allows us to study some of the kinetics during the processes applied. The three-phase co-existence and transitions between α-COA, β-COA and COM can be probed by fitting appropriate functions to these data. Limiting the fitting to the 140 °C step, an approximate isothermal case in an open capillary system, the time (t) evolution (growth) of the phase fraction (f) of α-COA can be described using the equation:

$$f = -16.4(3) + 0.371(6)t - 0.00121(2)t^2$$

with an adjusted coefficient of determination R^2 of 0.994. The reduction in COM has been fitted with both a linear and polynomial function, with the adjusted R^2 being 0.958 and 0.997 respectively. The polynomial showed a better fit and is given by:

$$f = 27.6(2) - 0.241(4)t - 0.00063(5)t^2$$

Finally the increase in the β-COA is clearly linear (adjusted R^2 of 0.983) with:

$$f = -0.065(8) + 0.00257(5)t$$

These relationships suggests that α- to β-COA is a zeroth order process with the rate constant given by 0.00257(5) min^{-1}, or as α-COA decreases in concentration, β-COA increases in concentration. In contrast, the COM to α-COA transition appears to be a second order process and this is consistent with the conversion from COM to α-COA requiring the production and removal of water. Thus two products are formed α-COA and H_2O in this open system experiment.

The final transition is the decomposition of β-COA. To track the phase evolution of the $CaCO_3$ another sequence of refinements has been undertaken from point "A" onwards in **Figure 3**c. In this case, the last dataset of the entire run has been used to refine the lattice and phase fractions of $CaCO_3$ in addition to the β-COA phase. Then this has been sequentially refined back to point "A" in **Figure 3**b. The phase fractions and lattice parameter evolution of these two phases are shown in **Figure 3**c. This shows essentially a two-phase reaction between the β-COA and $CaCO_3$ during the 370°C hold. Minor (if any) variations are observed in the lattice parameters of the $CaCO_3$ and β-COA, the largest being the slight contraction of *a* and *c* in the β-COA. Note the $CaCO_3$ lattice parameters prior to the 370°C temperature plateau show large errors, as there are minute quantities of this phase.

The phase evolution of calcium oxalate monohydrate during the heating cycles employed in the synchrotron XRD can be summarized as shown in Figure S2 of the Supplementary Information.

Thermodynamic stability

The next step in this work has been to computationally explore thermodynamic stability. The energy differences between the four COA phases examined here have been computed by using the five DFT functionals and the two basis sets mentioned in the previous sections. Results relative to β-COA are reported in **Table 3**. As expected,[51] due to the similarity in the density and crystallographic structures between β-COA, COA-III and COA-IV, all functionals and both basis sets provide very similar relative energy differences, with the order of stability β-COA > COA-IV >> COA-III. This is surprising, as α-COA in the experiments appears to fit well with COA-III. However, its reactivity and our inability to isolate this phase may be in part related to its lower stability compared to β-COA. In order to produce β-COA, water must be extracted from COM and the intermediate is likely to be COA-III as demonstrated in the experiments.

COA-II is also less stable than β-COA. However, the relative energy difference depends on the method due to short- and long-range correlation not being properly accounted for by DFT. While for the other three phases these interactions would tend to cancel due to fortuitous compensation of errors, this does not happen between β-COA and COA-II due to their major structural and density differences. For this reason, the values in **Table 3** range between +1.2 and +22.5 kJ/mol. Note that for a given functional and basis set, the uncertainty associated to these numbers is of the order of fractions of kJ/mol, and depends on computational parameters, approximations and algorithms adopted. While in all cases COA-II is less stable than β-COA and COA-IV, it is not

possible to establish on the basis of these calculations whether it is more or less stable than COA-III.

The thermodynamic stability of the four COA polymorphs as a function of temperature has been explored in the range of 0-800 K. The free energy differences are plotted as a function of temperature with respect to β-COA in **Figure 4**. Since all functionals and basis sets provide nearly the same trend for the β-COA, COA-III and COA-IV, only data obtained with PBE0 are reported in each figure, while for COA-II data obtained with five DFT functionals are reported.

As mentioned in the previous paragraphs, β-COA results in the most stable phase over the entire range of temperatures explored. This is in agreement with our experimental findings, where we observe either β-COA or α-COA that transforms into β-COA as soon as it is formed. While the stability of both COA-II and COA-IV with respect to β-COA decreases with temperature, though following different trends, the stability of COA-III increases. These results, though approximate (due to the assumptions of harmonic vibrations; constant volume over the entire range of temperature; only vibrational contribution to entropy included), provide a qualitative insight into the free energy trends of these phases. However, despite the fact that there seems to be no transition in **Figure 4** between phases β, III, and IV, given the opposite nature of the trends for COA-III and COA-IV, and the small energy difference between β-COA and COA-IV in the range of 0 to 150 K, we cannot, on the basis of these models, exclude the possibility that transitions may occur in the real sample.

Due to the nature of the COA-II phase, we are unable to make further predictions related to its stability. **Figure 4** indeed shows that while the slope of the free energy function is largely

independent of the functional and basis set, its position in the plot changes significantly, giving rise to very different predictions for transition temperatures.

Vibrational frequencies, infrared and Raman spectra analysis of COA polymorphs

The vibrational spectra of the four COA models have been calculated using the PBE0 functional and the V-BS basis set. To the best of our knowledge, the earliest measurement of the spectra of β-COA was reported by Shippey.[44] However, since no further experimental or computational vibrational spectra are available, the aim here is to provide some new information that can aid in the characterization of COA polymorphs.

The 3N-3 vibrational modes, N being the number of atoms in the unit cell, can be symmetry classified according to the following decomposition of the reducible representations (Γ) built on the basis of the Cartesian coordinates of the unit cell atoms for the four COA structures:

$\Gamma_{\beta\text{-COA}} = 15A_u \oplus 24B_u \oplus 24A_g \oplus 18B_g$

$\Gamma_{\text{COA-II}} = 81\ A$

$\Gamma_{\text{COA-III}} = 15A_u \oplus 24B_u \oplus 24A_g \oplus 18B_g$

$\Gamma_{\text{COA-IV}} = 7A_u \oplus 11B_u \oplus 12A_g \oplus 9B_g$

For COA-II, because it belongs to the space group *P*1 and has the lowest symmetry, all modes (81) are both IR and Raman active, although some IR intensities are actually equal to zero. In particular, as can be seen in Table S1 of the Supplementary Information, frequencies that have a high IR intensity have an almost zero Raman intensity and vice-versa, with the exception of some cases in the lattice mode region (<320 cm^{-1}). For the other three structures, as tabulated in

Table 4 and **Table 5**, all A_u and B_u modes are IR active (39 for β-COA and COA-III, 18 for COA-IV), while all A_g and B_g modes are Raman active (42 for β-COA and COA-III, 21 for COA-IV).

Figure 5 and **Figure 6** show that the IR and Raman spectra of the four phases present many common features, as expected from their very similar structures. The spectra can be divided into 6 and 7 distinct regions, respectively, which have been characterized through graphical analysis of the computed eigenvectors. Both spectroscopic methods allow detection of the asymmetric stretching mode region of the C-O bonds, ν_{as}(C-O), in the high frequency range at 1670-1770 cm^{-1}, which also exhibits the most intense bands. Similarly, the region of lattice modes below 320 cm^{-1} is present in both spectra. Raman spectra exhibit the following bands: 1480-1560 cm^{-1}, symmetric stretching of C-O bonds plus stretching of C-C bonds, ν_s(C-O)+ν(C-C); 915-970 cm^{-1}, ν(C-C); 860-880 cm^{-1}, out-of-plane O-C=O and C-C bending modes, δ(OCO)+δ(OCC); 600-620 cm^{-1}, δ(OCC); 500-530 cm^{-1}, ν(C-C)+δ(OCO). IR spectroscopy allow the detection of the following vibrational modes: 1350-1400 cm^{-1}, ν_s(C-O)+δ(OCO); 790-820 cm^{-1}, in-plane δ(OCO); 500-530 cm^{-1}, out-of-plane δ(OCO); 360-430, in-plane δ(OCC). These findings are in overall good agreement with the analysis provided by Shippey,[44] as well as with the data reported for other oxalate phases.[52]

Furthermore, various regions of the spectra in **Figure 5** and **Figure 6** show the high similarity between β-COA and COA-IV bands. **Table 4** and **Table 5** report the IR and Raman features of the four phases, and compare them to the observed values by Shippey.[44] For the reasons discussed in a previous paragraph, only frequencies higher than 300 cm^{-1} with non-zero intensity are reported in these tables for COA-II, whereas the full spectrum is shown in Table S1 of the

Supplementary Information. In **Table 4** and **Table 5**, the experimental frequencies are matched to the closest corresponding calculated vibrational frequencies value for comparison.

Most bands observed by Shippey[44] are in close proximity of groups of modes having a high calculated total intensity. Some predicted fundamental modes appear as bands with very low intensity and were not observed in Shippey's[44] experiments. Computed modes in the high frequency region (mostly associated with C-O stretching), above 1300 cm^{-1}, are a few tens of cm^{-1} overestimated with respect to the corresponding bands observed by Shippey.[44] While this could be due to the experimental challenge of correctly assigning modes falling within a band as broad as that shown in Figure 5(a) for Shippey's IR spectrum, the IR spectrum recorded in this study (Figure S3 in the Supplementary Information) and Shippey's Raman spectrum show that the bands in the high frequency region are clearly slightly red-shifted with respect to our prediction for all phases. The adopted basis set and computational parameters have been shown to provide deviations of at most ±10 cm^{-1} in most minerals. Anharmonicity is also known to account for more than a few cm^{-1} only for those modes involving H atoms. From tests performed on $CaCO_3$ aragonite, which has well known spectral features,[29,53] the C-O stretching modes are overestimated by as much as 50 cm^{-1} when the PBE0 functional is used, whereas all the other modes are in good agreement with the experimental values. This is therefore the likely reason for the apparent disagreement observed between computed and measured spectra of COA in the C-O stretching region.

The quality and availability of experimental data on COA does not allow a more accurate comparison between experimental and computed spectra. As for the comparison between the four COA polymorphs, **Figure 5** and **Figure 6** show that despite the many spectral similarities,

differences can be observed in terms of number of peaks and width of the bands, some of which may possibly be detected through advanced spectroscopic techniques.

Conclusions

This paper confirms that at least another polymorph exists for COA other than the one known as β-COA. The structure of this phase, namely α-COA, is here determined for the first time, through applying *ab initio* methods coupled with *in situ* synchrotron XRD data. Structural analysis and thermodynamic phase stability, as obtained through theoretical modeling have ultimately led to the prediction of three new possible atomic arrangements for the COA polymorphs, in addition to β-COA, with the latter turning out to be the energetically favored phase over the full range of temperatures examined. However, on the basis of these models, we cannot exclude the possibility that phase transitions may occur if other factors are involved in the real sample, and this is clearly evidenced in the experimental data. The latter show that two distinct phases of COA are formed during dehydration of COM, namely α- and β- phases, despite the fact that α-COA cannot be isolated from the other phases. It is also shown that the structure of α-COA corresponds to one of those theoretically derived in this paper, namely COA-III. The existence of a third γ-phase cannot be confirmed on the basis of our experiments. Indeed, this phase was observed only once as a result of dehydration of COD, and only on finely ground samples.[23] With the aim of providing reference data for future experiments aimed at studying COA polymorphism, IR and Raman spectra have been computed for the four models and compared between each other and with existing experimental measurements. They exhibit very similar features, due to extreme structural similarities, but some differences in number and

position of peaks can be observed that may allow structural models to be discriminated between in future studies.

ASSOCIATED CONTENT

Supporting Information. Rietveld refined fit to COM at room temperature; phase evolution of COM; IR spectra measured in this work; full set of IR and Raman active modes for COA-II.

AUTHOR INFORMATION

Corresponding Author

*Raffaella Demichelis (Raffaella.demichelis@curtin.edu.au)

Author Contributions

WZ, PR, JDG and RD have run and analyzed all the calculations. WZ, NS, FJ have performed and interpreted the experiments. The manuscript was written through contributions of all authors. All authors have given approval to the final version of the manuscript.

Funding Sources

Australian Research Council Discovery Programme (FT130100463, DE160100237 and DP160100677)

ACKNOWLEDGMENT

WZ would like to thank the China Scholarship Council (CSC)-Curtin International Postgraduate Research Scholarship (CIPRS) Scheme for a joint PhD scholarship; NS, PR, JDG, and RD would like to thank the Australian Research Council for funding through DE160100237, FT130100463, and DP160100677; RD also thanks Curtin University for an Early Career

Research Fellowship. This work was supported by resources provided by the Pawsey Supercomputing Centre and the National Computational Infrastructure (NCI) with funding from the Australian Government and the Government of Western Australia. The authors also thank the Australian Synchrotron for access to the beamline (AS152/PD/9303).

Figure 1. Optimized structures of COA viewed along the *b* lattice parameter and comparison of their calculated XRD patterns in the range of $5 \leq 2\theta \leq 40^{o}$ with $\lambda = 0.99996$ Å. Calcium is represented in green, carbon in grey and oxygen atoms within the oxalate group in red; water molecules in COM (also oriented along the *b* lattice parameter) are shown in light blue. Blue lines represent the unit cell edges.

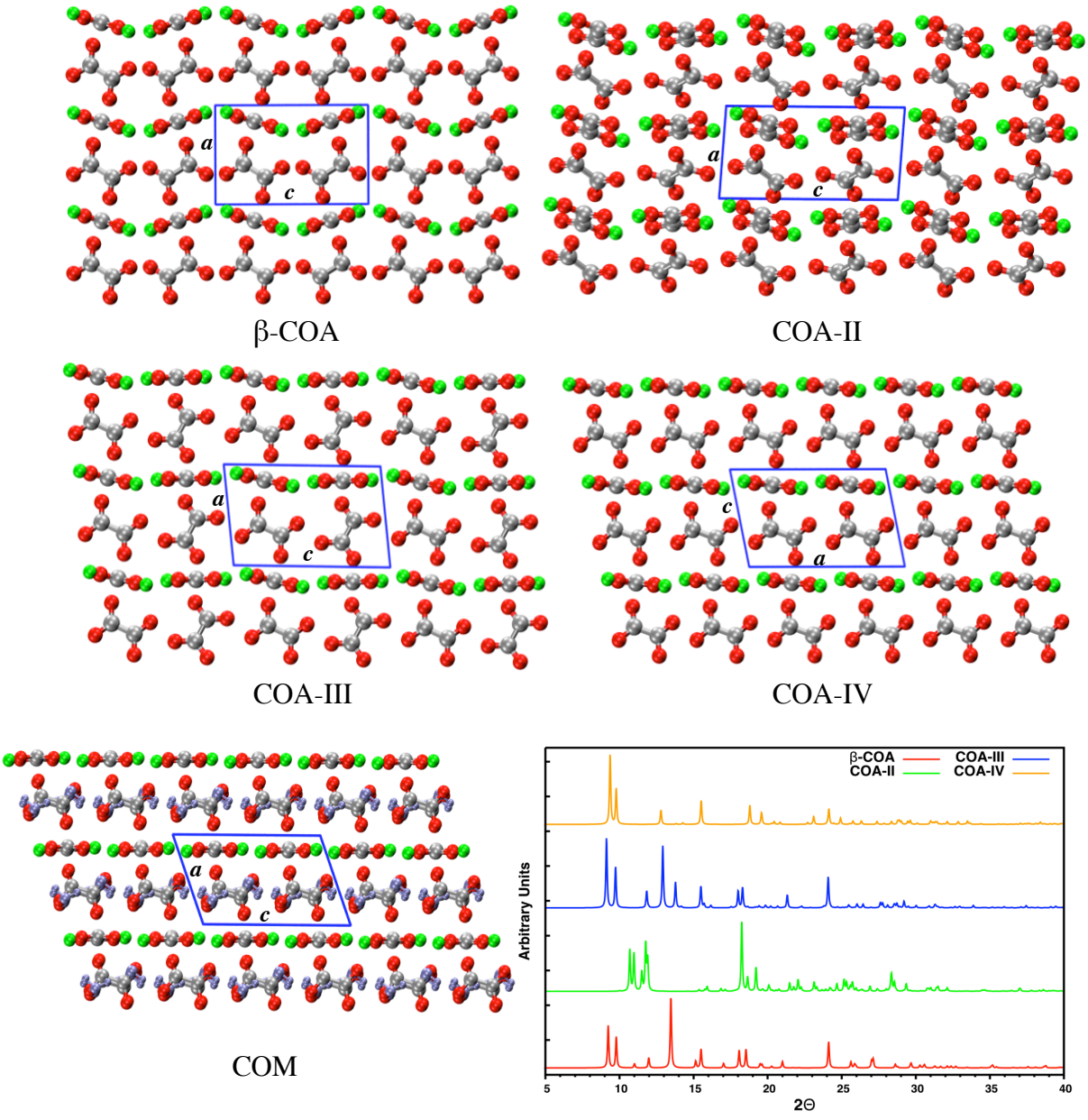

Figure 2. Selected 2θ regions of variable temperature synchrotron XRD data highlighting the phase evolution, with (a)-(c) detailing the first experiment while (d)-(e) details the second experiment. The color scale shows intensity variation, the heating profile appears on the right and the phases are labeled according to the text. In (a) the temperature-time region at the start of the experiment up to 360ºC; (b) and (c) the whole experiment and different 2θ ranges.

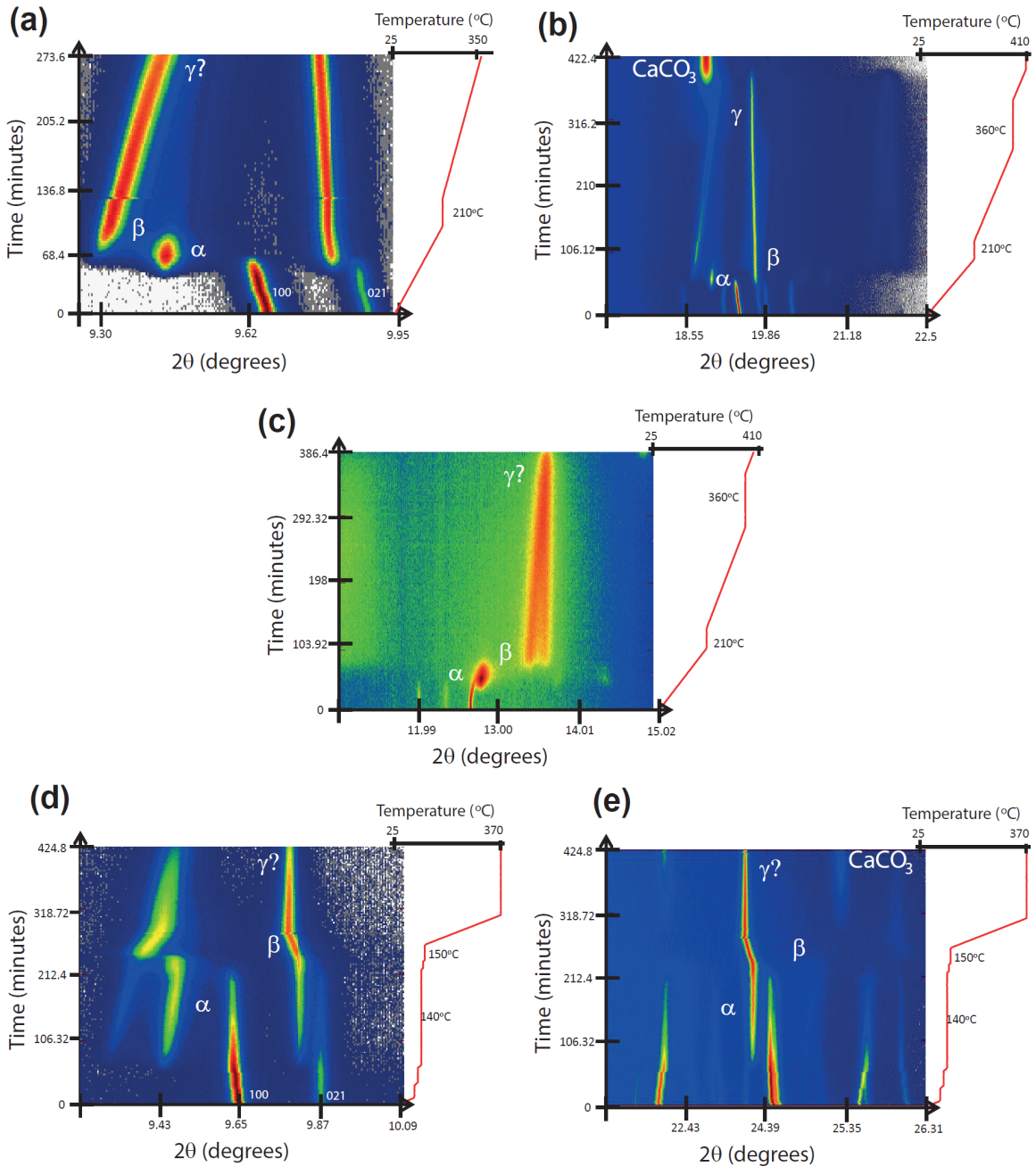

Figure 3. (a) Evolution of selected reflections assigned to the various initial phases from Rietveld analyses. (b) Rietveld refined fit of the COM, COA-III and β-COA models to the synchrotron XRD data at 140 °C. The top portion shows an enlarged region. Data are shown as crosses, the calculated Rietveld model as a line through the data, and the difference between the data and the model as the line below the data. The vertical reflection markers are labeled for the phase present from top to bottom are COA-III, β-COA and COM and $\chi^2 = 2.26$ with 19 refined parameters. (c)-(d) Parameters are derived from Rietveld refinements as a function of time, with the temperature profile included (red, top panel in c, d). (c) The evolution of the lattice parameters and phase fractions of the COM (black squares bottom four panels), "β" phase (β-COA) (blue middle 4 panels) and at the top 3 panels are the phase fractions. Note A and B are discussed in the text. (d) The evolution of the lattice parameters and phase fractions of the β-COA and $CaCO_3$.

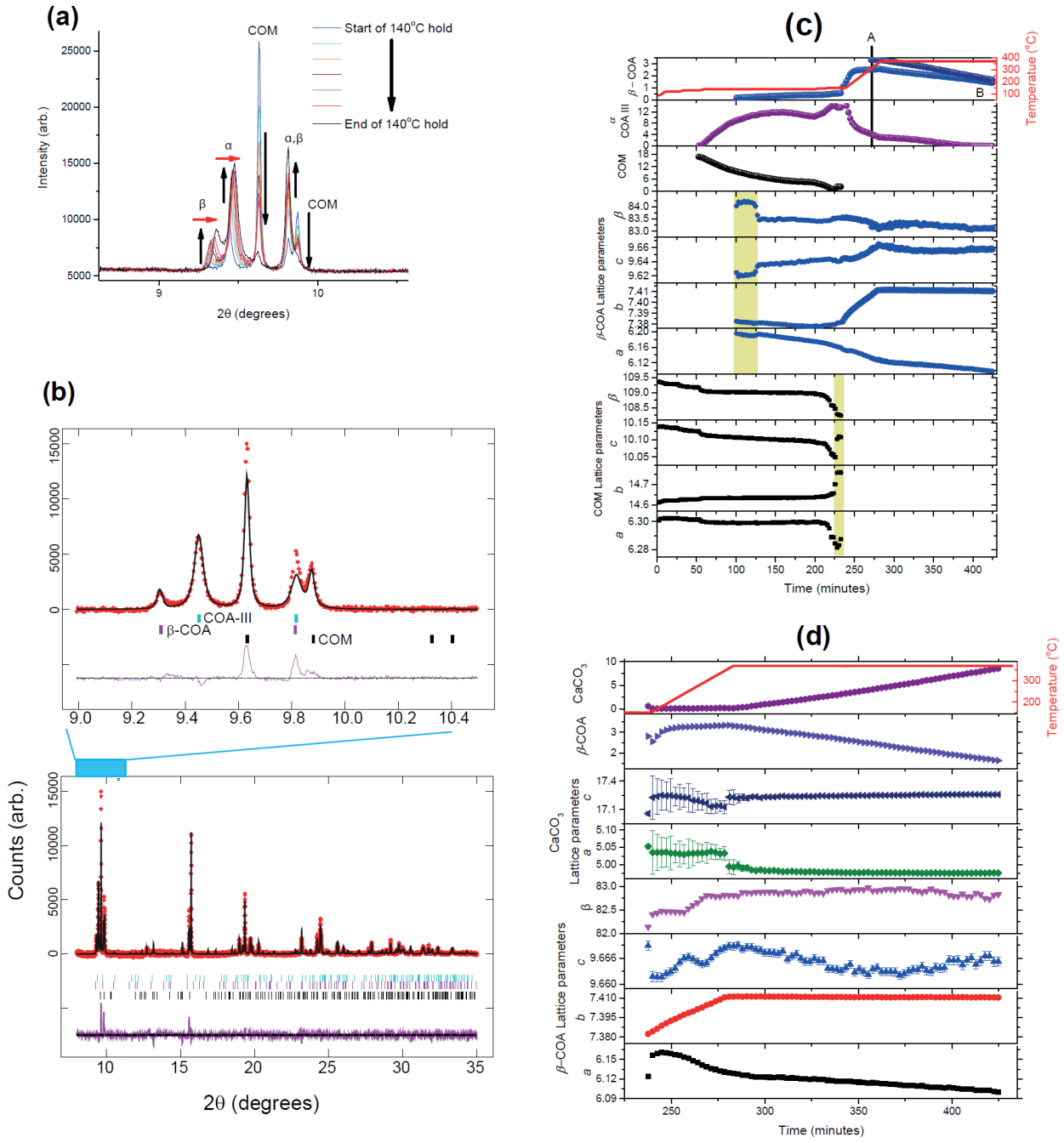
(a)
Start of 140°C hold
End of 140°C hold
COM
α
α,β
β
COM
Intensity (arb.)
2θ (degrees)
(b)
COA-III
β-COA
COM
Counts (arb.)
2θ (degrees)
(c)
A
B
Temperature (°C)
β−COA
α COA III
COM
β-COA Lattice parameters
COM Lattice parameters
Time (minutes)
(d)
CaCO3
β-COA
CaCO3 Lattice parameters
β-COA Lattice parameters
Temperature (°C)
Time (minutes)

Figure 4. Free energy difference as a function of temperature, ΔG(T), between the alternative COA structures and β-COA: (a) V-BS basis set; (b) pob_TZVP basis set. The trends for COA-III and COA-IV with the five functionals nearly overlap, therefore only data for PBE0 are reported; data obtained with all the considered functionals are reported for COA-II.

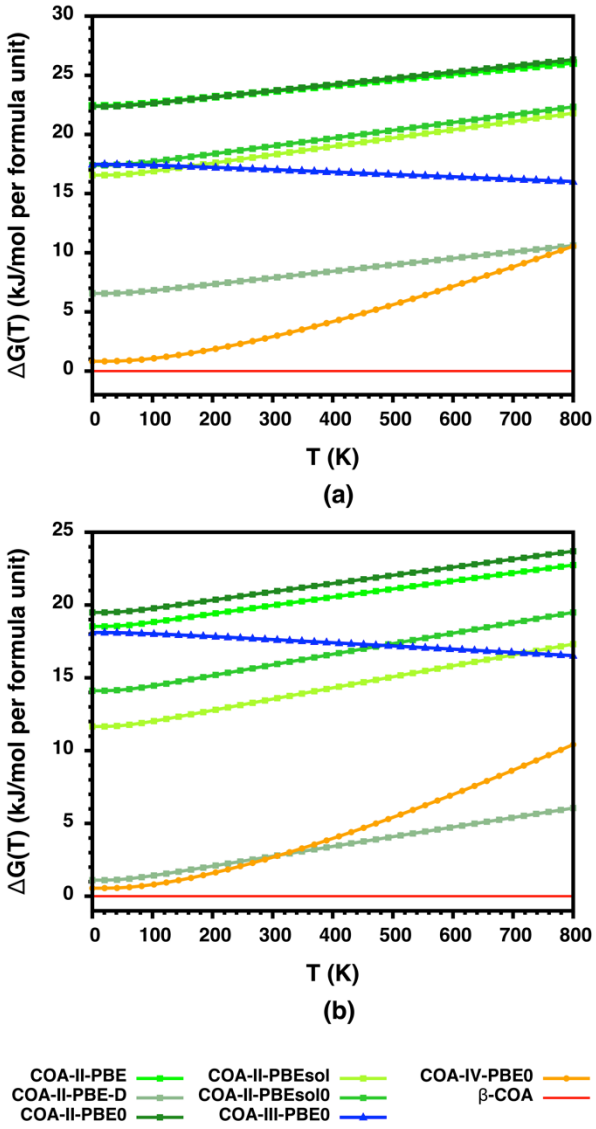

Figure 5. Comparison between experimental (digitalized from the work of Shippey[44]) and computed IR spectra of COA polymorphs. Simulated IR spectra are raw absorbance spectra and Lorentzian peaks have been calculated from the integrated intensities I and frequencies ν displayed in **Table 4** and Table S1 of the Supplementary Information, with a step size of 1 cm^{-1} and damping factor of 8 cm^{-1}. (a) Full spectra; (b-d) zoom on different regions.

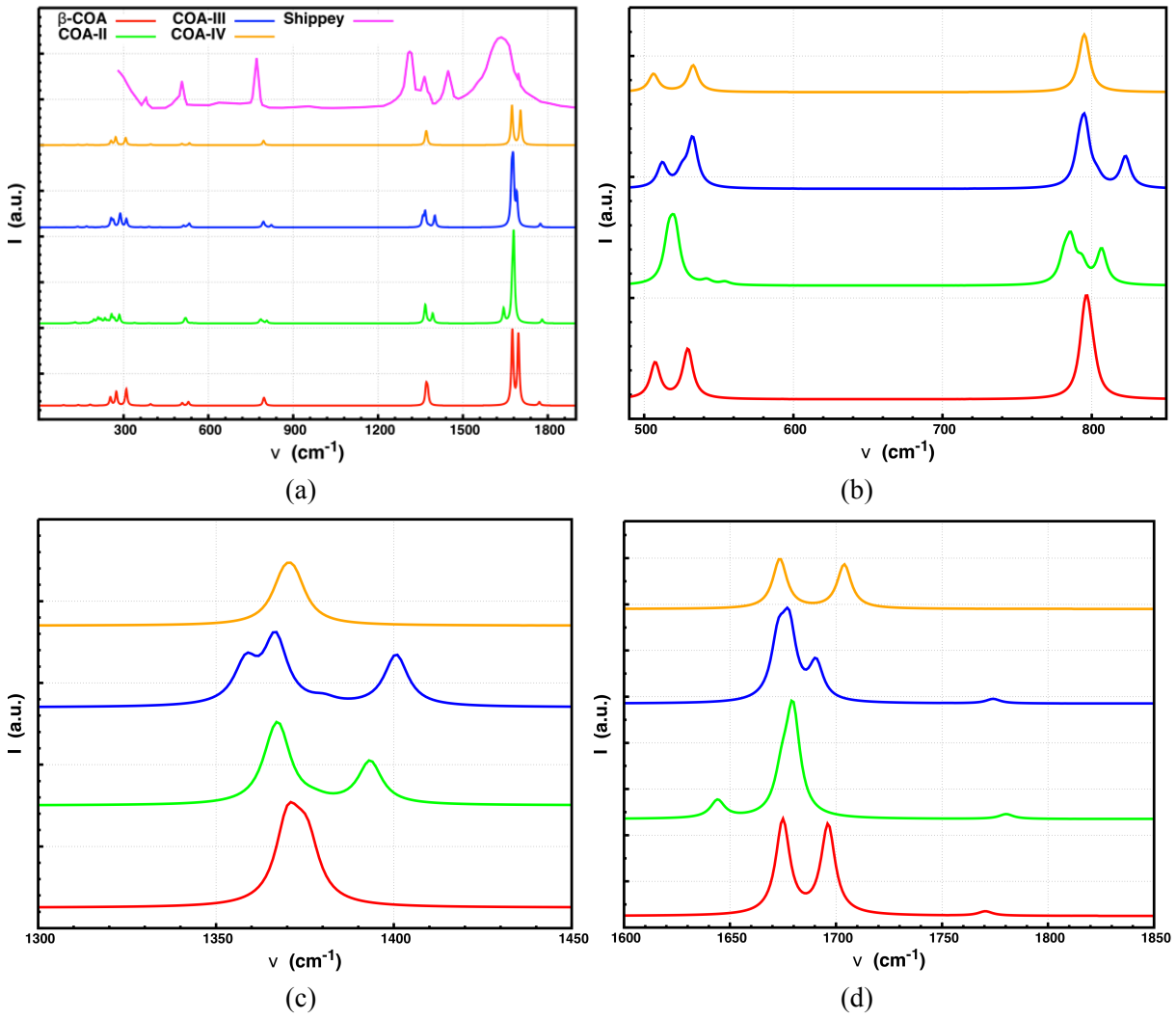

Figure 6. Comparison between experimental (digitalized from the work of Shippey[44]) and computed Raman spectra of COA polymorphs. Simulated Raman spectra produced as in **Figure 5**, with ν and I from **Table 5** and Table S1 of the supplementary information, with a laser wavelength of 514.5 nm,[44] a temperature of 300 K and a damping factor of 10 cm^{-1}. (a) Full spectra; (b-d) zoom on different regions.

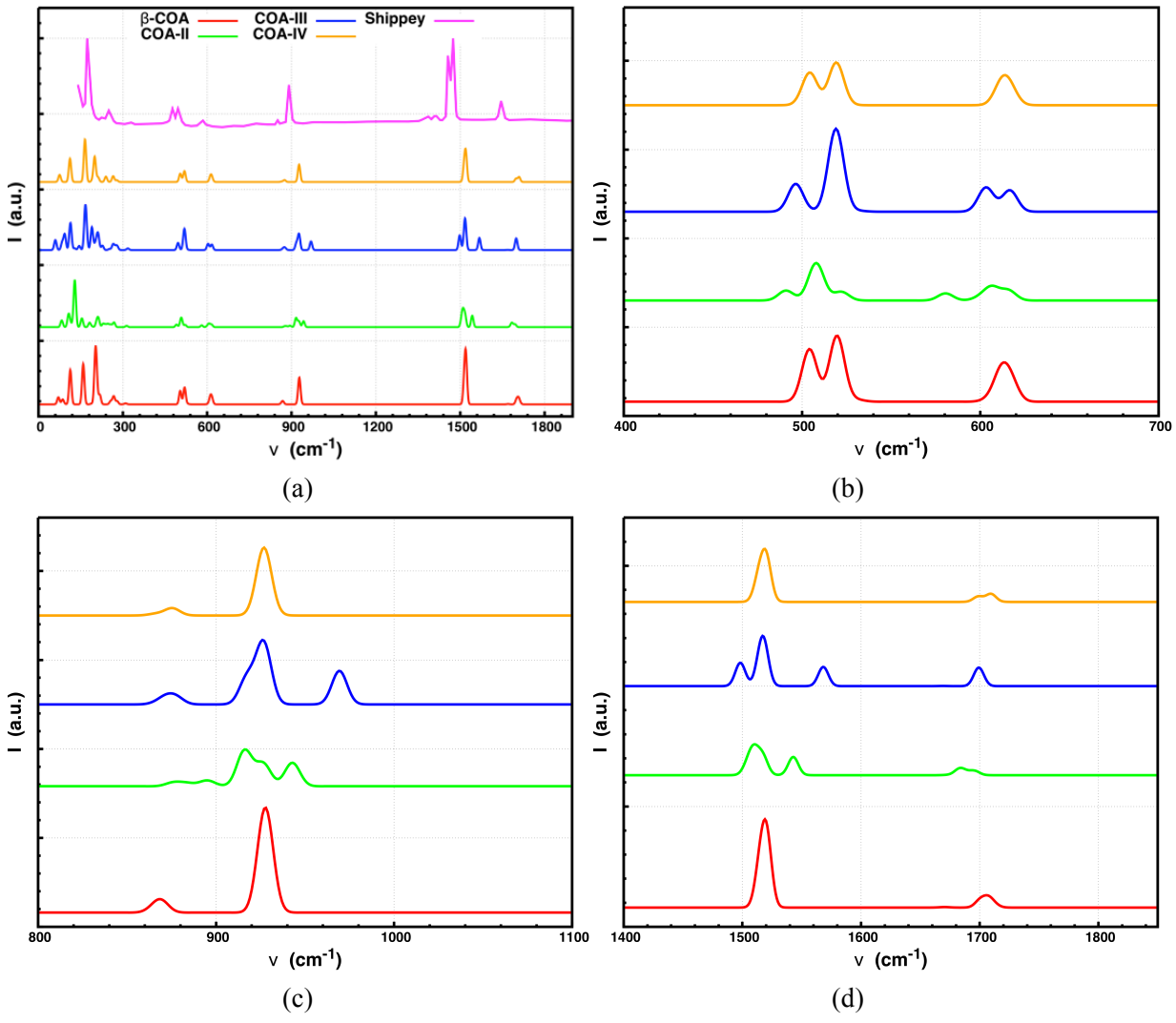

Table 1. Optimized structural parameters of β-COA (P2/*m*) obtained by using five different functionals and two basis sets. a, b and c lattice parameters are in Å; β in degrees. The volume V is in Å^3 and the density ρ is in g/cm^3.

	V-BS					pob_TZVP					Hochrein *et al*[25]	
	PBE	PBEsol	PBE0	PBEsol0	PBE-D	PBE	PBEsol	PBE0	PBEsol0	PBE-D	PBE	Rietveld Refined
a	6.249	6.184	6.209	6.162	6.211	6.274	6.212	6.234	6.188	6.236	6.247	6.164
b	7.481	7.368	7.414	7.332	7.413	7.494	7.386	7.423	7.343	7.429	7.515	7.362
c	9.639	9.556	9.586	9.525	9.599	9.690	9.605	9.626	9.565	9.649	9.653	9.537
β	90.01	90.00	89.97	89.97	90.00	89.99	90.00	90.00	89.99	90.00	90.12	90.24
V	450.62	435.39	441.26	430.33	441.94	455.62	440.68	445.46	434.63	446.98	453.13	432.83
ρ	1.886	1.952	1.926	1.975	1.923	1.865	1.928	1.908	1.955	1.901	1.875	1.966

Table 2. Optimized structural parameters of the four COA phases (V-BS, PBE0). Units and symbols are as per **Table 1**. The optimized structure of COM is also reported for sake of comparison.

	β-COA	COA-II	COA-III	COA-IV	COM
Space group	P2/*m*	P1	P2/*m*	C2/*m*	$P2_1/c$
a	6.209	6.145	6.321	9.762	6.338
b	7.414	7.249	7.419	7.409	14.681
c	9.586	9.681	9.753	6.222	10.100
α	90	91.69	90	90	90
β	89.97	93.00	83.96	100.21	109.26
γ	90	121.41	90	90	90
V	441.26	366.72	454.81	442.95	887.34
ϱ	1.926	2.317	1.868	1.919	2.185

Table 3. Relative energies of the three hypothetical COA polymorphs with respect to β-COA ($kJ \cdot mol^{-1}$ per formula unit).

	V-BS					pob-TZVP				
	PBE	PBEsol	PBE0	PBEsol0	PBE-D	PBE	PBEsol	PBE0	PBEsol0	PBE-D
$U_{E\ COA\text{-}II}$	+22.5	+16.4	+22.3	+17.1	+6.5	+18.7	+11.7	+19.6	+14.1	+1.2
$U_{E\ COA\text{-}III}$	+17.5	+17.1	+17.6	+17.3	+19.6	+17.7	+17.7	+18.4	+18.4	+19.8
$U_{E\ COA\text{-}IV}$	+1.7	+1.2	+1.4	+0.9	+1.4	+1.2	+0.9	+1.1	+0.9	+0.8

Table 4. Comparison of calculated and experimental IR-active vibrational frequencies (ν, cm^{-1}) and intensities (I, $Km \cdot mol^{-1}$) for COA phases. For all COA polymorphs, the three translational modes are excluded from this table. Symmetry assignment (Sym) of the modes for β-COA, COA-III and COA-IV is the same (the sequential order of values in italic font in COA-III has been changed in order to match the modes of β-COA). All modes for COA-II have A symmetry, so only modes with intensity greater than 1 are reported here. The lattice mode region in COA-II is excluded from this table.

		β-COA		COA-III		COA-IV		COA-II		Exp.[44]
n	Sym	ν	I	ν	I	ν	I	ν	I	ν
1	B_u	61.0	1	59.6	<1					
2	A_u	87.8	42	62.9	12	87.1	18			
3	A_u	90.6	<1	90.2	9					
4	B_u	94.2	<1	91.4	<1					
5	B_u	99.1	<1	101.8	<1					
6	B_u	140.0	49	*138.5*	*39*	138.6	30			
7	A_u	145.5	<1	*134.4*	*18*					
8	A_u	152.8	5	165.6	<1					
9	B_u	168.9	<1	*170.3*	*<1*	163.8	<1			
10	A_u	177.1	<1	*169.4*	*70*	170.7	37			
11	A_u	182.0	74	187.3	17	189.6	9			
12	A_u	211.4	<1	209.5	1					
13	B_u	217.4	7	224.5	30					
14	A_u	252.3	2	252.3	17					
15	A_u	253.4	561	256.0	538	256.0	282			
16	B_u	272.8	2	263.8	416	272.3	538			
17	B_u	274.4	948	285.5	255					280 *m*
18	B_u	307.5	166	288.9	768	307.5	496			
19	B_u	310.1	997	310.1	554					
20	B_u	395.5	108	360.2	24	396.0	59	339.1	35	392 *mw*

21	B_u	402.4	3	389.9	44			389.6	15	
22	B_u	418.3	<1	417.0	<1			408.4	2	
23	B_u	432.7	<1	429.1	15	432.6	<1	424.1	6	
24	A_u	507.4	186	512.2	124	506.3	93	516.5	217	
25	A_u	515.3	<1	525.4	70			520.7	254	
26	B_u	527.4	26	530.8	11			542.0	22	524 *m*
27	B_u	529.5	237	532.6	243	532.8	138	554.2	15	
28	B_u	794.6	209	791.9	156	794.0	153	781.5	111	
29	A_u	797.1	334	795.5	287	795.9	164	785.9	204	787 *s*
30	B_u	800.9	100	*822.6*	*162*			793.4	93	
31	A_u	803.3	<1	*803.4*	*42*			806.6	179	
32	A_u	1370.0	1103	*1366.7*	*1031*	1368.9	555	1365.7	426	1320 *s*
33	B_u	1372.7	290	*1358.4*	*626*	1372.1	569	1367.8	914	1360 *vw*
34	B_u	1375.8	825	*1400.6*	*791*			1377.7	51	
35	A_u	1382.0	<1	*1380.3*	*81*			1393.3	660	1390 *vw*
36	B_u	1674.9	5131	1672.7	3065	1673.5	2707	1644.1	966	1636 *vs*
37	B_u	1696.0	1761	1677.8	3778	1703.9	2388	1674.5	1925	
38	B_u	1696.3	3108	1690.6	2007			1679.7	5727	1709 *vw*
39	B_u	1770.4	238	1774.1	244			1780.3	258	

Table 5. Comparison of calculated and experimental Raman-active vibrational frequencies (ν, cm^{-1}) and intensities (I, arbitrary units) for COA phases. For the reported modes in COA-II and the values in italic font in COA-III, see caption in **Table 4** for details.

		β-COA		COA-III		COA-IV		COA-II		Exp.[44]
n	Sym	ν	I	ν	I	ν	I	ν	I	ν
1	B_g	70.8	2	60.0	3	75.1	3			
2	B_g	86.1	2	84.4	4					
3	B_g	94.5	<1	93.5	11					101 *vs*
4	B_g	113.1	18	113.7	26	112.1	20			
5	B_g	129.3	<1	128.8	2					
6	A_g	158.1	3	144.9	6					153 *vs*
7	A_g	159.2	36	166.7	81	165.4	70			
8	A_g	188.6	<1	171.8	12	191.6	3			
9	B_g	202.3	59	190.0	53	199.9	57			193 *vs*
10	B_g	205.4	<1	*209.2*	*27*					
11	A_g	206.0	34	*202.0*	*14*					
12	B_g	218.0	16	213.1	27	212.0	11			
13	A_g	255.2	2	227.5	14	240.0	16			
14	A_g	258.0	5	252.8	4					
15	B_g	267.4	17	265.4	23	265.6	21			
16	B_g	271.4	2	*280.0*	*16*					
17	A_g	280.0	8	*273.4*	*12*	278.6	7			
18	A_g	309.7	3	317.8	9			313.4	12	301
19	A_g	504.2	39	496.5	71	504.3	75	491.0	42	487
20	A_g	504.2	38	517.5	73			507.1	106	509
21	A_g	519.6	100	519.7	158	519.2	102	509.3	66	
22	A_g	531.0	3	531.8	2			522.0	40	
23	B_g	604.6	4	*604.6*	*2*			580.5	38	595
24	A_g	611.4	27	*601.5*	*21*	611.9	61	599.9	16	
25	A_g	611.8	26	*603.7*	*59*			606.4	73	
26	B_g	617.1	37	616.5	73	616.8	44	615.7	57	

27	B_g	864.8	4	867.0	8	866.2	8	876.0	34	860
28	B_g	865.0	7	871.7	17			883.5	28	
29	B_g	869.2	32	872.3	19			893.7	21	
30	B_g	869.6	<1	877.7	36	875.4	34	895.8	34	
31	A_g	923.8	<1	917.3	144			915.9	304	901
32	A_g	926.9	213	923.6	26	926.5	251	916.5	35	
33	A_g	927.3	15	926.8	332	928.1	94	926.5	215	
34	A_g	929.3	117	969.3	202			942.8	231	
35	A_g	1513.9	157	1498.3	604	1513.9	544	1504.6	427	1467
36	A_g	1515.1	395	1514.8	401			1509.9	1000	1480
37	A_g	1518.9	22	1518.0	1000			1517.3	805	
38	A_g	1520.5	1000	1568.2	529	1520.1	1000	1542.9	832	
39	B_g	1670.3	9	1668.8	6			1673.3	13	1648
40	B_g	1700.2	123	1698.8	236	1698.8	145	1682.9	305	
41	A_g	1707.2	158	1699.3	282			1687.8	114	
42	A_g	1712.7	39	1700.6	55	1709.5	217	1695.6	218	1724

REFERENCES

(1) Knoll, A. H. Biomineralization and Evolutionary History. *Rev Mineral Geochem* **2003**, *54*, 329–356.

(2) Mann, S. Biomineralization and Biomimetic Materials Chemistry. *J. Mater. Chem.* **1995**, *5*, 935–946.

(3) Bäuerlein, *E. Biomineralization: Progress in Biology, Molecular Biology and Application*, 2nd ed.; Wiley-VCH Verlag GmbH, Weinheim Germany, 2004.

(4) Sterling, C. Crystal Structure of Weddellite. *Science (New York, N.Y.)* **1964**, *146*, 518–519.

(5) Graustein, W. C.; Cromack, K.; Sollins, P. Calcium Oxalate: Occurrence in Soils and Effect on Nutrient and Geochemical Cycles. *Science* **1977**, *198*, 1252–1254.

(6) Stephens, W. E. Whewellite and Its Key Role in Living Systems. *Geol Today* **2012**, *28*, 180–185.

(7) Daudon, M.; Bazin, D.; Andre, G.; Jungers, P.; Cousson, A.; Chevallier, P.; Veron, E.; Matzen, G. Examination of Whewellite Kidney Stones by Scanning Electron Microscopy and Powder Neutron Diffraction Techniques. *J Appl Cryst* **2009**, *42*, 109–115.

(8) Bowers, G. M.; Kirkpatrick, R. J. Natural Abundance ^{43}Ca NMR as a Tool for Exploring Calcium Biomineralization: Renal Stone Formation and Growth. *Cryst. Growth Des.* **2011**, *11*, 5188–5191.

(9) Orlando, M. T. D.; Kuplich, L.; de Souza, D. O.; Belich, H.; Depianti, J. B.; Orlando, C. G. P.; Medeiros, E. F.; da Cruz, P. C. M.; Martinez, L. G.; Corrêa, H. P. S.; et al. Study of Calcium Oxalate Monohydrate of Kidney Stones by X-Ray Diffraction. *Powder Diffr.* **2012**, *23*, 59–64.

(10) Khan, S. R. Reactive Oxygen Species as the Molecular Modulators of Calcium Oxalate Kidney Stone Formation: Evidence From Clinical and Experimental Investigations. *J. Urol.* **2013**, *189*, 803–811.

(11) Rodgers, A. L.; Webber, D.; Ramsout, R.; Gohel, M. D. I. Herbal Preparations Affect the Kinetic Factors of Calcium Oxalate Crystallization in Synthetic Urine: Implications for Kidney Stone Therapy. *Urolithiasis*. **2014**, *42*, 221–225.

(12) Daudon, M.; Bazin, D.; Letavernier, E. Randall's Plaque as the Origin of Calcium Oxalate Kidney Stones. *Urolithiasis*. **2015**, *43*, 5–11.

(13) Dunmire, B.; Harper, J. D.; Cunitz, B. W.; Lee, F. C.; Hsi, R.; Liu, Z.; Bailey, M. R.; Sorensen, M. D. Use of the Acoustic Shadow Width to Determine Kidney Stone Size with Ultrasound. *J. Urol.* **2016**, *195*, 171–177.

(14) Rusakov, A. V.; Frank-Kamenetskaya, O. V.; Gurzhiy, V. V.; Zelenskaya, M. S.; Izatulina, A. R.; Sazanova, K. V. Refinement of the Crystal Structures of Biomimetic Weddellites Produced by Microscopic Fungus Aspergillus Niger. *Crystallogr. Rep.* **2014**, *59*, 362–368.

(15) Tazzoli, V.; Domeneghetti, C. The Crystal Structure of Whewellite and Weddellite: Re-Examination and Comparison. *Am. Mineral.* **1980**, *65*, 327–334.

(16) Deganello, S.; Kampf, A. R.; Moore, P. B. The Crystal Structure of Calcium Oxalate Trihydrate: $Ca(H_2O)_3(C_2O_4)$. *Am. Mineral.* **1981**, *66*, 859–865.

(17) Deganello, S. The Structure of Whewellite, $CaC_2O_4 \cdot H_2O$, at 328 K. *Acta Cryst.* **1981**, *B37*, 826–829.

(18) Blom, N. S.; Kanters, J. A. Calcium Oxalate Trihydrate, $CaC_2O_4 \cdot 3h_2O$. *Cryst. Struct. Comm.* **1981**, *10*, 1283–1288.

(19) Basso, R.; Lucchetti, G.; Zefiro, L.; Palenzona, A. Caoxite, $Ca(H_2O)_3(C_2O_4)$, A New Mineral From the Cerchiara Mine, Northern Apennines, Italy. *N. Jb. Fur Miner. Mh.* **1997**, *2*, 84–96.

(20) Echigo, T.; Kimata, M.; Kyono, A.; Shimizu, M.; Hatta, T. Re-Investigation of the Crystal Structure of Whewellite $[Ca(C_2O_4) \cdot H_2O]$ and the Dehydration Mechanism of Caoxite $[Ca(C_2O_4) \cdot 3h_2O]$. *Mineral. Mag* **2005**, *69*, 77–88.

(21) Gehl, A.; Dietzsch, M.; Mondeshki, M.; Bach, S.; Häger, T.; Panthöfer, M.; Barton, B.; Kolb, U.; Tremel, W. Anhydrous Amorphous Calcium Oxalate Nanoparticles From Ionic Liquids: Stable Crystallization Intermediates in the Formation of Whewellite. *Chem. Eur. J.* **2015**, *21*, 18192–18201.

(22) Hajir, M.; Graf, R.; Tremel, W. Stable Amorphous Calcium Oxalate: Synthesis and Potential Intermediate in Biomineralization. *Chem. Commun.* **2014**, *50*, 6534.

(23) Walter-Lévy, L.; Laniepce, J. *C. R. Acad. Sc. Paris* **1964**, *259*, 4685–4688.

(24) Hocart, R.; Watelle-Marion, G.; Thrierr-Sorel, A.; Gérard, N. *C. R. Acad. Sc. Paris*

1965, *260*, 2363–2366.

(25) Hochrein, O.; Thomas, A.; Kniep, R. Revealing the Crystal Structure of Anhydrous Calcium Oxalate, $Ca[C_2O_4]$, By a Combination of Atomistic Simulation and Rietveld Refinement. *Z. anorg. allg. Chem.* **2008**, *634*, 1826–1829.

(26) Dovesi, R.; Orlando, R.; Erba, A.; Zicovich-Wilson, C. M.; Civalleri, B.; Casassa, S.; Maschio, L.; Ferrabone, M.; La Pierre, De, M.; D'Arco, P.; et al. CRYSTAL14: a Program for the Ab Initio Investigation of Crystalline Solids. *Int. J. Quantum Chem.* **2014**, *114*, 1287–1317.

(27) Valenzano, L.; Torres, F. J.; Doll, K.; Pascale, F.; Zicovich-Wilson, C. M.; Dovesi, R. Ab Initio Study of the Vibrational Spectrum and Related Properties of Crystalline Compounds; the Case of $CaCO_3$ Calcite. *Z. Phys. Chem.* **2006**, *220*, 893–912.

(28) Valenzano, L.; Noël, Y.; Orlando, R.; Zicovich-Wilson, C. M.; Ferrero, M.; Dovesi, R. Ab Initio Vibrational Spectra and Dielectric Properties of Carbonates: Magnesite, Calcite and Dolomite. *Theor Chem Account* **2007**, *117*, 991–1000.

(29) La Pierre, De, M.; Carteret, C.; Maschio, L.; André, E.; Orlando, R.; Dovesi, R. The Raman Spectrum of $CaCO_3$ Polymorphs Calcite and Aragonite: a Combined Experimental and Computational Study. *J. Chem. Phys.* **2014**, *140*, 164509.

(30) Demichelis, R.; Raiteri, P.; Gale, J. D.; Dovesi, R. The Multiple Structures of Vaterite. *Cryst. Growth Des.* **2013**, *13*, 2247–2251.

(31) Peintinger, M. F.; Oliveira, D. V.; Bredow, T. Consistent Gaussian Basis Sets of Triple-Zeta Valence with Polarization Quality for Solid-State Calculations. *J. Comput. Chem.*

2012, *34*, 451–459.

(32) Weigend, F.; Ahlrichs, R. Balanced Basis Sets of Split Valence, Triple Zeta Valence and Quadruple Zeta Valence Quality for H to Rn: Design and Assessment of Accuracy. *Phys. Chem. Chem. Phys.* **2005**, *7*, 3297.

(33) Weigend, F.; Haser, M.; Patzelt, H.; Ahlrichs, R. RI-MP2: Optimized Auxiliary Basis Sets and Demonstration of Efficiency. *Chem Phys Lett* **1998**, *294*, 143–152.

(34) Perdew, J. P.; Burke, K.; Ernzerhof, M. Generalized Gradient Approximation Made Simple. *Phys. Rev. Lett.* **1996**, *77*, 3865–3868.

(35) Perdew, J.; Ruzsinszky, A.; Csonka, G.; Vydrov, O.; Scuseria, G.; Constantin, L.; Zhou, X.; Burke, K. Restoring the Density-Gradient Expansion for Exchange in Solids and Surfaces. *Phys. Rev. Lett.* **2008**, *100*, 136406(1-4).

(36) Adamo, C.; Barone, V. Toward Reliable Density Functional Methods Without Adjustable Parameters: the PBE0 Model. *J. Chem. Phys.* **1999**, *110*, 6158–6170.

(37) Grimme, S. Semiempirical GGA-Type Density Functional Constructed with a Long-Range Dispersion Correction. *J. Comput. Chem.* **2006**, *27*, 1787–1799.

(38) Dovesi, R.; Saunders, V. R.; Roetti, C.; Orlando, R.; Zicovich-Wilson, C. M.; Pascale, F.; Civalleri, B.; Doll, K.; Harrison, N. M.; Bush, I. J.; et al. CRYSTAL14 User's Manual. **2014**, 1–382.

(39) Pack, J. D.; Monkhorst, H. J. Special Points for Brillouin-Zone Integrations. *Phys. Rev. B* **1976**, *13*, 5188–5192.

(40) Ferrero, M.; Rérat, M.; Orlando, R.; Dovesi, R. The Calculation of Static Polarizabilities of 1-3D Periodic Compounds. the Implementation in the Crystal Code. *J. Comput. Chem.* **2008**, *29*, 1450–1459.

(41) Ferrero, M.; Rérat, M.; Kirtman, B.; Dovesi, R. Calculation of First and Second Static Hyperpolarizabilities of One- to Three-Dimensional Periodic Compounds. Implementation in the CRYSTAL Code. *J. Chem. Phys.* **2008**, *129*, 244110.

(42) Maschio, L.; Kirtman, B.; Rérat, M.; Orlando, R.; Dovesi, R. Ab Initio Analytical Raman Intensities for Periodic Systems Through a Coupled Perturbed Hartree-Fock/Kohn-Sham Method in an Atomic Orbital Basis. I. Theory. *J. Chem. Phys.* **2013**, *139*, 164101.

(43) Maschio, L.; Kirtman, B.; Rérat, M.; Orlando, R.; Dovesi, R. Ab Initio Analytical Raman Intensities for Periodic Systems Through a Coupled Perturbed Hartree-Fock/Kohn-Sham Method in an Atomic Orbital Basis. II. Validation and Comparison with Experiments. *J. Chem. Phys.* **2013**, *139*, 164102.

(44) Shippey, T. A. Vibrational Studies of Calcium Oxalate Monohydrate (Whewellite) and an Anhydrous Phase of Calcium Oxalate. *J. Mol. Struct.* **1980**, *63*, 157–166.

(45) Macrae, C. F.; Edgington, P. R.; McCabe, P.; Pidcock, E.; Shields, G. P.; Taylor, R.; Towler, M.; van de Streek, J. Mercury: Visualization and Analysis of Crystal Structures. *J Appl Crystallogr* **2006**, *39*, 453–457.

(46) Wallwork, K. S.; Kennedy, B. J.; Wang, D. The High Resolution Powder Diffraction Beamline for the Australian Synchrotron; AIP, 2007; Vol. 879, pp 879–882.

(47) Larson, A. C.; Dreele, Von, R. B. General Structure Analysis System (GSAS). *Los Alamos National Laboratory Report LAUR* **1994**, 86–748.

(48) Toby, B. H. EXPGUI, a Graphical User Interface for GSAS. *J Appl Cryst* **2001**, *34*, 210–213.

(49) Demichelis, R.; Raiteri, P.; Gale, J. D.; Dovesi, R. Examining the Accuracy of Density Functional Theory for Predicting the Thermodynamics of Water Incorporation Into Minerals: the Hydrates of Calcium Carbonate. *J. Phys. Chem. C* **2013**, *117*, 17814–17823.

(50) Demichelis, R.; Civalleri, B.; D'Arco, P.; Dovesi, R. Performance of 12 DFT Functionals in the Study of Crystal Systems: Al_2SiO_5 Orthosilicates and Al Hydroxides as a Case Study. *Int. J. Quantum Chem.* **2010**, *110*, 2260–2273.

(51) Casassa, S.; Demichelis, R. Relative Energy of Aluminum Hydroxides: the Role of Electron Correlation. *J. Phys. Chem. C* **2012**, *116* (24), 13313–13321.

(52) Frost, R. L.; Weier, M. L. Raman Spectroscopy of Natural Oxalates at 298 and 77 K. *J. Raman Spectrosc.* **2003**, *34*, 776–785.

(53) Carteret, C.; La Pierre, De, M.; Dossot, M.; Pascale, F.; Erba, A.; Dovesi, R. The Vibrational Spectrum of $CaCO_3$ Aragonite: a Combined Experimental and Quantum-Mechanical Investigation. *J. Chem. Phys.* **2013**, *138*, 014201.

For Table of Content use only

Anhydrous Calcium Oxalate Polymorphism: a combined computational and synchrotron X-ray diffraction study.

Wen Zhao, Neeraj Sharma, Franca Jones, Paolo Raiteri, Julian D. Gale, Raffaella Demichelis

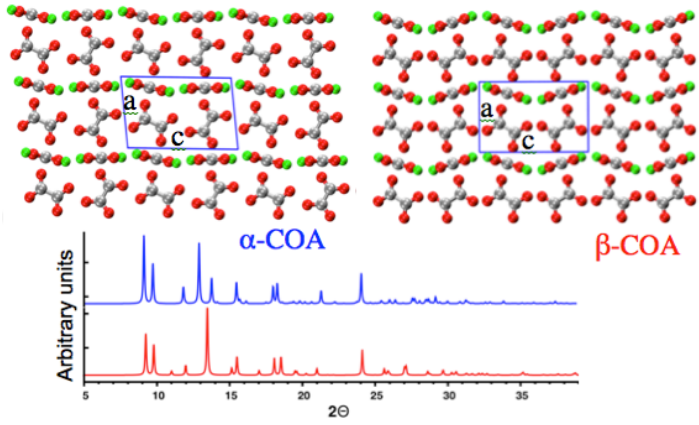

The α-polymorph of anhydrous calcium oxalate has been characterized through *ab initio* computational methods and *in situ* synchrotron X-ray diffraction.

Supplementary Information

Anhydrous Calcium Oxalate Polymorphism: a combined computational and synchrotron X-ray diffraction study.

Wen Zhao[1], Neeraj Sharma[2], Franca Jones[3], Paolo Raiteri[1], Julian D. Gale[1], Raffaella Demichelis[1,]*

[1]Curtin Institute for Computation and Department of Chemistry, Curtin University, GPO Box U1987, Perth, Western Australia 6845, Australia [2]School of Chemistry, University of New South Wales, Sydney, New South Wales, Australia.

[3]Nanochemistry Research Institute and Department of Chemistry, Curtin University, GPO Box U1987, Perth, Western Australia 6845, Australia.

*raffaella.demichelis@curtin.edu.au

Figure S1. Rietveld refined fit of the COM model to the synchrotron XRD data. The top portion shows an enlarged region. Data are shown as crosses, the calculated Rietveld model as a line through the data, and the difference between the data and the model as the line below the data. The vertical reflection markers are labeled for the phase present.

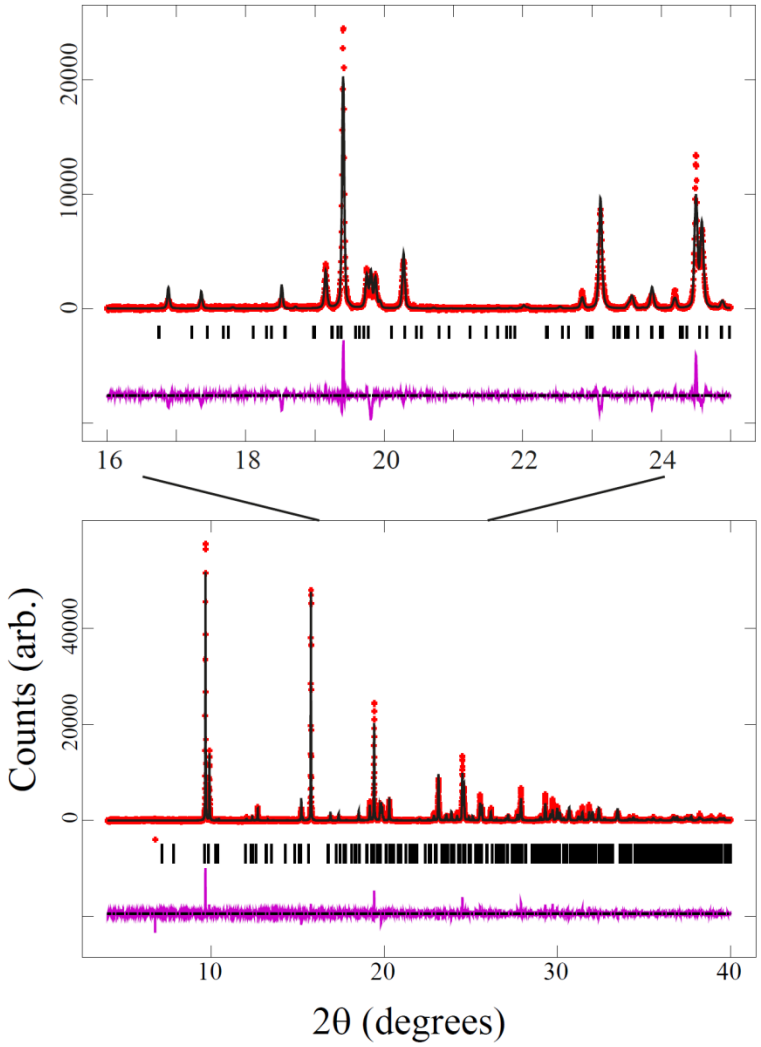

Figure S2. Schematic illustrating the evolution of reaction mechanisms observed during heating with the different colors of shading indicating the distinct regions.

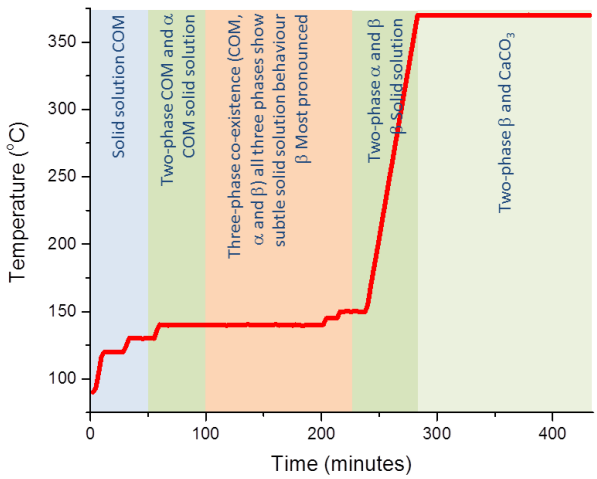

Figure S3. Infrared spectrum of COA formed at 142 °C by heating COM in oven for 48 hours. Obtained at 2 cm^{-1} resolution, 64 scans, diamond ATR on a Nicolet IS50 FTIR.

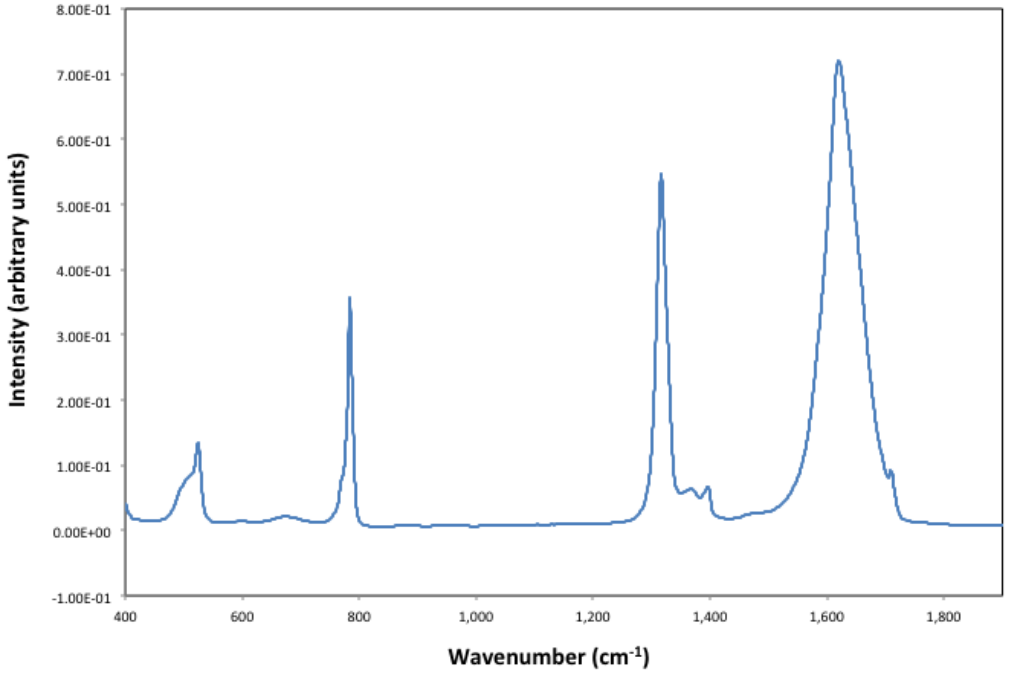

Figure S4. Thermogravimetric analysis of the calcium oxalate sample.

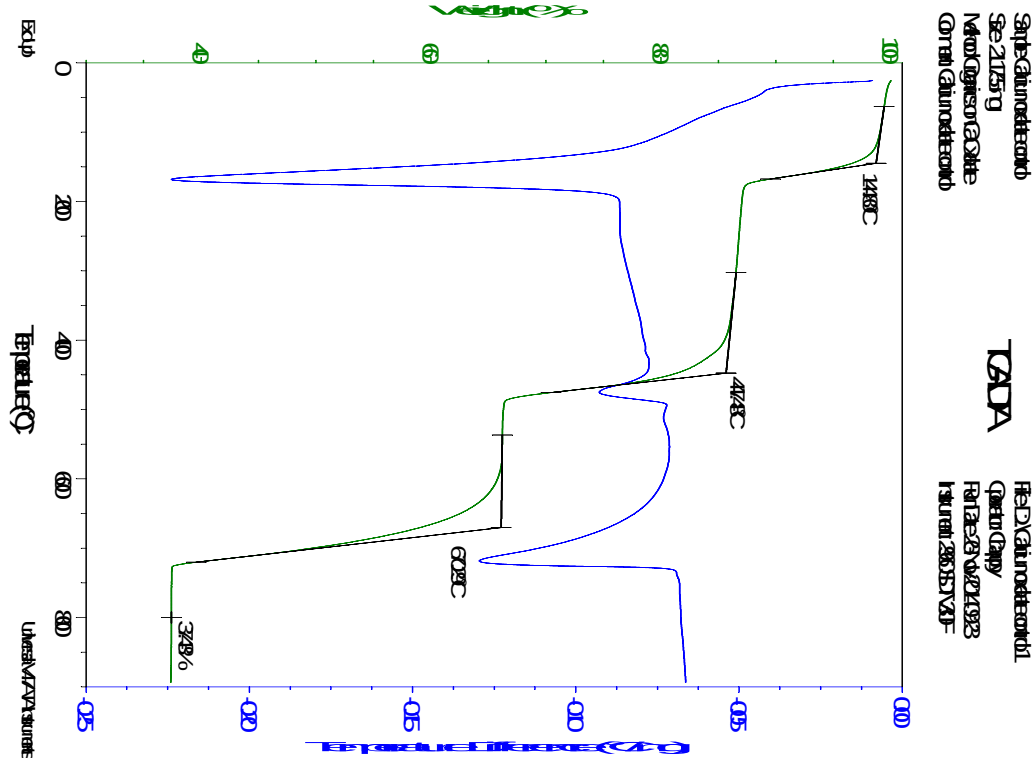

Table S1 Calculated vibrational frequencies (ν, cm^{-1}), infrared integrated intensities (I_{IR}, $Km \cdot mol^{-1}$) and Raman integrated intensities (I_{Raman}, given in arbitrary units) for COA-II. All modes for COA-II have A symmetry.

n	ν	I_{IR}	I_{Raman}	n	ν	I_{IR}	I_{Raman}	n	ν	I_{IR}	I_{Raman}
1	82.6	<1	6	28	238.6	<1	15	55	785.9	204	<1
2	85.0	<1	<1	29	243.8	127	<1	56	793.4	93	<1
3	107.3	<1	19	30	247.4	<1	12	57	806.6	179	<1
4	113.2	11	<1	31	248.0	<1	6	58	876.0	<1	34
5	115.1	<1	5	32	257.4	63	15	59	883.5	<1	28
6	121.8	20	<1	33	257.5	506	2	60	893.7	<1	21
7	128.9	61	10	34	266.9	293	<1	61	895.8	<1	34
8	129.0	7	88	35	268.7	<1	33	62	915.9	<1	304
9	148.2	1	<1	36	285.3	569	<1	63	916.5	<1	35
10	153.2	<1	3	37	313.4	<1	12	64	926.5	<1	215
11	154.6	<1	22	38	339.1	35	<1	65	942.8	<1	231
12	155.8	20	<1	39	389.6	15	<1	66	1365.7	426	<1
13	164.1	23	<1	40	408.4	2	<1	67	1367.8	914	<1
14	181.6	<1	16	41	424.1	6	<1	68	1377.7	51	<1
15	185.0	71	<1	42	491.0	<1	42	69	1393.3	660	<1
16	190.5	<1	2	43	507.1	<1	106	70	1504.6	<1	427
17	195.4	227	<1	44	509.3	<1	66	71	1509.9	<1	1000
18	205.0	74	<1	45	516.5	217	<1	72	1517.3	<1	805
19	207.1	<1	22	46	520.7	254	<1	73	1542.9	<1	832
20	210.3	317	<1	47	522.0	<1	40	74	1644.1	966	<1
21	211.9	<1	17	48	542.0	22	<1	75	1673.3	<1	13
22	212.4	16	<1	49	554.2	15	<1	76	1674.5	1925	<1
23	214.0	<1	23	50	580.5	<1	38	77	1679.7	5727	<1
24	219.9	235	<1	51	599.9	<1	16	78	1682.9	<1	305
25	226.5	22	<1	52	606.4	<1	73	79	1687.8	<1	114
26	229.7	<1	18	53	615.7	<1	57	80	1695.6	<1	218
27	234.1	299	<1	54	781.5	111	<1	81	1780.2	258	<1